Nano Research
2023, 16(12): 12901–12909
ISSN 1998-0124 CN 11-5974/O4
https://doi.org/10.1007/s12274-023-5590-5

Research Article

Design and optical performance investigation of all-sprayable ultrablack coating

Chen Shen[1,2,§], Huiyong Li[1,3,§], Shuai Sun[1,2], Hui Zhang[1] (✉), Lanqin Yan[1], and Zhong Zhang[1,4] (✉)

[1] *CAS Key Laboratory of Nanosystem and Hierarchical Fabrication, CAS Center for Excellence in Nanoscience, National Center for Nanoscience and Technology, Beijing 100190, China*
[2] *University of Chinese Academy of Sciences, Beijing 100049, China*
[3] *Key Lab of Organic Optoelectronics and Molecular Engineering of Ministry of Education Laboratory of Flexible Electronics Technology, Department of Chemistry, Tsinghua University, Beijing 100084, China*
[4] *CAS Key Laboratory of Mechanical Behavior and Design of Materials, Department of Modern Mechanics, University of Science and Technology of China, Hefei 230027, China*
[§] *Chen Shen and Huiyong Li contributed equally to this work.*

Received: 26 December 2022 / **Revised:** 15 February 2023 / **Accepted:** 19 February 2023

ABSTRACT

Although ultrablack surfaces are urgently needed in wide applications owing to their extremely low reflectance over a broadband wavelength, obtaining simultaneously the ultrablackness and mechanical robustness by simple process technique is still a great challenge. Herein, by decoupling different light extinction effects to different layers of coating, we design an ultrablack coating that is all-sprayable in whole process. This coating presents low reflectance over visible–mid-infrared (VIS–MIR) wavelength (av. $R \approx 1\%$ in VIS), low multi-angle scattering (bidirectional reflection distribution function (BRDF) = 10^{-2}–10^{-3} sr^{-1}), together with good substrate adhesion grade and self-cleaning ability, which are superior to most reported sprayable ultrablack surfaces. The light extinction effects of each layer are discussed. This method is also applicable in other material systems.

KEYWORDS

ultrablack, spray-coating, carbon nanomaterials, multiple scattering, intermediate layer

1 Introduction

The ultrablack materials have attracted intense attention over the past decades, owing to their extraordinary light absorption performance from visible to infrared wavelength. Numerous optical applications urgently need ultrablack materials for stray light suppression [1, 2], infrared detection [3, 4], solar energy harvesting [5–9], and stealth technology [10–12], etc. Previous work found the materials having only 1% difference of light absorption resulted in at least 1 order of magnitude difference of stray light level [13], indicating the importance of high absorptive materials.

Researchers have proposed various strategies to fabricate ultrablack materials artificially over the past decades. Building of micro/nano-sized morphologies [6, 14–21] on flat surfaces to form micro/nano light trapping structures is the common way to improve the light absorption of these surfaces. Typical technologies to establish these light traps involve chemical/physical vapor deposition [22], chemical etching [23], micromachining [24], laser processing [16], and template processing [21]. Representatives are the vertically aligned carbon nanotube (VACNT) array [15, 25], black silicon [26], and black gold [27]. Another strategy is based on Fresnel effect, which indicates as light travels on the interface of air and material surface, interface reflection unavoidably occurs due to the abrupt change in refractive index (RI) of media [28, 29]. To suppress the interfacial light reflection, one or several intermediate layers can be introduced on the surface [30, 31]. The intermediate should have a RI between those of substrate surface and air; it can be constructed by fabricating some low-density porous materials [32–36] or deposition of multi-layer coatings [37–39].

While significant progress has been made over the past decades, there are still some drawbacks for the present ultrablack materials for their real and largescale applications. First, most of the present methods are complicated and time-consuming, some materials need to be prepared at high temperature and/or vacuum. For example, the VACNT needs to grow at the temperature higher than 450 °C, which cannot be withstood by thermolabile substrates. Besides, the ultrablack materials, due to their elaborate micro/nano-structures on surfaces and/or high filler fraction, usually have poor abrasion resistance and lower adhesion with substrates, which do not meet the requirements of routine operations, such as touch, cleaning, wear, and slight tension or bending. It is still a considerable challenge to achieve the ultrablack materials combining excellent light absorption, good mechanical robustness as well as simple and efficient processing technology simultaneously.

Herein, considering different light extinction effects, which included intrinsic absorption of carbon nanomaterials, multiple scattering of hollow microspheres, and anti-interfacial reflection of intermediate layer, we designed and prepared a sprayable

Address correspondence to Hui Zhang, zhangh@nanoctr.cn; Zhong Zhang, zhongzhang@ustc.edu.cn

ultrablack coating and analyzed the related light absorption mechanisms. This ultrablack coating can be applied to the parts with large area and/or complex curved surface by spray-coating method [40–42] only and then thermo-cured without the aid of any complicated equipment and harsh process conditions, and in principle, is more compatible with the current technological process, compared with the complicated techniques mentioned-above. The resulting coating exhibited excellent light reflection properties around 1% over a wide wavelength range from 400 to 2000 nm and approached 2% reflection in mid-infrared range of 2–20 μm, ensuring high-performance solar energy harvesting. Also, the coating processed good adhesion grade and self-cleaning performance. With the excellent performance and simple/scalable spray-coating in all processes, the ultrablack coating should find wide applications in practice.

2 Experimental

2.1 Materials

Carbon black (CB) nanoparticles with ~ 13 nm diameter (FW200) were obtained from Evonik Industries AG. Butyl acetate dispersion of single-walled CNTs (SWCNTs) was purchased from Chengdu Organic Chemistry Co., Ltd; the content of carbon nanotubes was about 0.2 wt.%–0.3 wt.%, and the amount of dispersant was about 3–4 times the weight of the SWCNTs. Surfactant (Triton X-100) was purchased from Shanghai Aladdin Biochemical Technology Co., Ltd. Polydimethylsiloxane (PDMS) (Sylgard 184) was purchased from Dow corning Co., Ltd. Epoxy resin (E51) was purchased from Nantong Xingchen Synthetic Material Co., Ltd. Methylhexahydrophthalic anhydride served as the hardener. 1H,1H,2H,2H-Perfluorodecyltrimethoxysilane (PFMS), butyl acetate (BuAc), and ethanol were purchased from Shanghai Macklin Biochemical Technology Co., Ltd. SiO_2 hollow microsphere (HMS) was provided by Forsman Technology Co., Ltd. (Beijing, China).

2.2 Preparation of CB/SWCNT/HMS/PDMS in BuAc dispersion

Figure 1 illustrates the general fabrication route of CB/SWCNT/HMS/PDMS in BuAc dispersion. Typically, 10 g SWCNTs in BuAc dispersion was weighed, diluted with 20 mL pure BuAc, added with SiO_2 HMS (0.1–0.4 g), and then mechanically stirred, the resulting dispersion was named as dispersion A. 0.4 g CB was dispersed in PDMS (0.5–4 g) with a vacuum deformer (Thinky, Japan) for 5 min, diluted with BuAc (to swell PDMS), and dropwise added with a few drops of Triton X-100. The dispersion was ultrasonically treated (Scientz-750F, Ningbo Scientz Biotechnology Co., Ltd) for 10 min, named as solution B. It should be mentioned that the relatively mild mixing condition was needed for dispersing of HMS, since HMS was easy to break during mixing, while the intensive mixing condition was used for CB to break up the CB agglomerates. Finally, the dispersions A and B were mixed together at desired ratio using a homogenizer at 2000 r/min for 2 h, obtaining CB/SWCNT/HMS/PDMS in BuAc dispersion.

2.3 Spray-coating process

As illustrated in Fig. 1, the CB/SWCNT/HMS/PDMS in BuAc dispersion was sprayed to substrate for five cycles under 0.4 MPa of air pressure using a spray gun (Prexi Hardware Tools Co., Ltd, nozzle diameter 0.5 mm) and was thermo-cured in oven at 80 °C for 2 h. Subsequently, PFMS in ethanol solution was spray-coated onto the cured surface for several cycles, then cured in a humidity chamber at 50 °C, 70% relative humidity (RH) for 2 h. Table S1 in the Electronic Supplementary Material (ESM) summarizes the information of the major samples in this work.

2.4 Characterization

The morphologies and elemental analysis of samples were measured by scanning electron microscopy (SEM) with an energy disperse spectroscopy (Hitachi, SU8220) and confocal microscopy (LHL-DCM8, Heyuan Tiandi Instrument Co., Ltd). The hemispherical reflectance spectra including specular and diffused reflection were measured by an ultraviolet–visible–near infrared ray (UV–VIS–NIR) spectrophotometer (Perkin Elmer, Lambda 950) equipped with a 150 mm integrating sphere. The spectral range was 400–2000 nm, and the angle of incidence was 8°. The hemispherical reflectance in infrared region (2–20 μm) was measured by a Fourier transform infrared (FT-IR) spectrometer (Vertex 80V, Bruker) equipped with an integrating sphere. The scattering performance of the sample (4 cm × 4 cm) was measured by a scattering characteristic measuring instrument (Suzhou Super Optics Technology, Inc, MWS5). Especially, the type of scattering

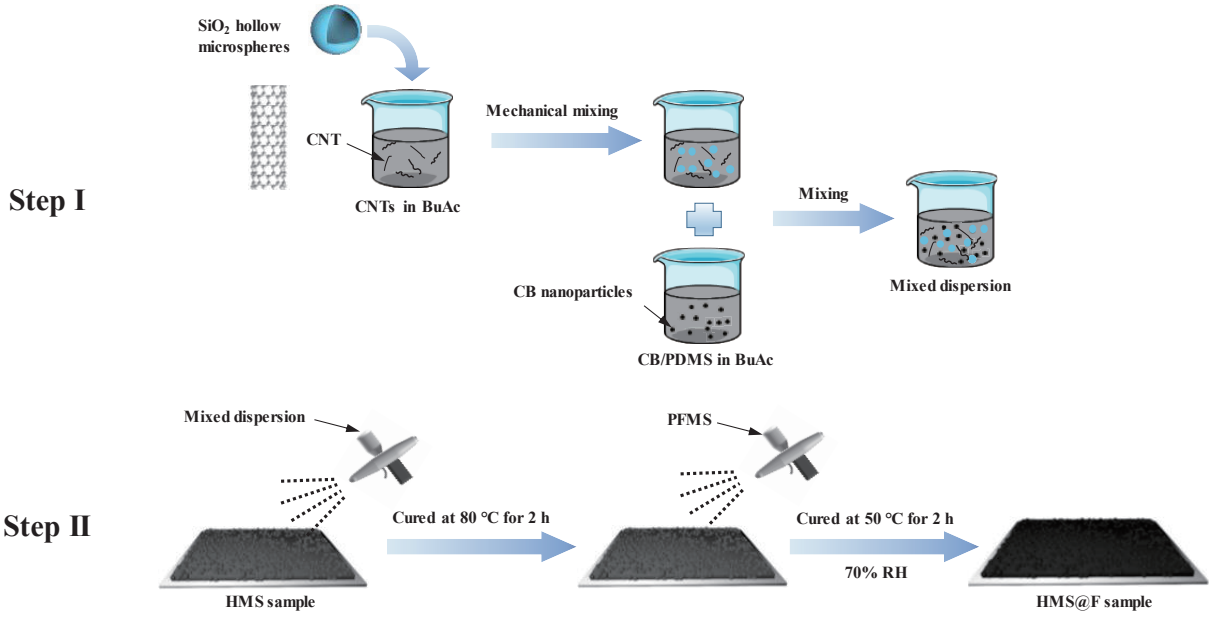

Figure 1 The schematic showing the fabrication route for all-sprayable ultrablack coating.

characteristic measuring was in the incident plane, and angles of incidence were 0°, 45°, and 75°. The diameter of the circular light source was 3 mm, while the wavelength of the light source was 532 nm. The refractive index was measured by a spectroscopic ellipsometer (SENTECH Co., Ltd, SE 850 DUV), and the curve was fitted by Cauchy model. Cross-cut adhesion grade between coating and substrate was measured referring to ISO 2409 standard. Solar simulator (Solar MH2500, NMERRY Co., Ltd) was used to illuminate samples, and IR camera (Fluke TiX560, Germany FLUKE corporation) was introduced to monitor the temperature of sample surface. Water contact angle and sliding angle were measured by a contact angle system (DSA100, Kruss Germany).

3 Results and discussion

It is well known that reflection, refraction, and subsequent absorption happen when light reaches a material surface (Fig. 2(a)). To minimize the reflected light and achieve the ultra-blackness, several light extinction effects could be utilized, as illustrated in Fig. 2(b): i) improving the intrinsic light absorption of materials, ii) constructing micro/nano light traps so as to form multiple scattering in these structures, and iii) introducing anti-interfacial reflective intermediate layer. Even though these effects have been tried before, combining them and realizing ultra-blackness in a sprayable coating have been a big challenge and have never been reported to the best of our knowledge.

Therefore, we tried to prepare the all-sprayable ultrablack coating sample taking advantage of aforementioned effects. Figure 1 illustrates the general fabrication route. Here, both CB particles and SWCNTs were selected as the light absorbers. The SiO_2 HMS was used to build the micro light traps. The PFMS acted as the low RI intermediate. In the first step, a certain amount of CB, SWCNT, HMS, and PDMS were carefully mixed in BuAc to form a homogeneous dispersion, which was subsequently sprayed onto a substrate and thermo-cured. In the second step, the PFMS in ethanol was sprayed onto the bottom layer and thermo-cured again. The detailed fabrication route is described in Experimental Section 2.2. All the process is effective and simple, and does not need any complicated equipment or harsh processing conditions. The roles played by different components in the coating will be discussed as follows.

Fresnel law indicates interfacial reflection exists as light propagates from air to a medium with RI value higher than air; the larger difference of RI between air and medium, the higher the light reflection [29]. Figure 3(a) compares the reflectance values calculated by Fresnel law with the experimental ones of some candidate polymer surfaces. The PDMS surface shows the lowest reflectance due to the lowest RI (Fig. 3(b)), as expected; additionally, it also shows good flexibility, high transparency, and good sprayability, therefore the PDMS was selected as the film-forming resin in this work.

Some nanoparticles have very good visible light absorbability. Figure 3(c) compares absorption coefficients (Q_{abs}) of C, Au, Ni, and Si individual nanoparticles (10 nm in diameter) calculated by Mie theory. The carbon nanoparticle exhibits a broadband high Q_{abs} over the wavelength of 300–800 nm; moreover, the Q_{abs} value is not sensitive to the wavelength change, differing from the Q_{abs} sharp drop of Au or Si nanoparticles at longer wavelength. Since the carbon nanoparticle (like CB) has much lower density and lower price, and is more available [43] than other nanoparticles, it is an ideal nano-absorber in this work. On the other hand, it is reported that as the gaps between nanoparticles are very small, tiny resonance cavities [44, 45] are built up, which enhance the light forward scattering and diminish light reflection. Our finite-difference time-domain (FDTD) simulation results, as shown in Fig. 3(d) and Video ESM1, confirm this enhanced forward scattering when carbon nanoparticles (10 nm in diameter, 1–5 nm interparticle distance) are used.

Figure S2 in the ESM calculates the absorption of PDMS coatings filled with carbon nanoparticles, the values of which depend on the radius, and volume fraction of nanoparticles and absorption depth (coating thickness). The carbon nanoparticles are very effective light absorber in the wavelength studied, in most cases, they are able to absorb the light entering the coating nearly completely.

The reason of selection of the SWCNTs is that a small amount of the SWCNTs is not only a good light absorber, but also works as the good connector in polymer matrix (owing to formation of the network structure), which improves the wear resistance and favors formation of a uniform layer [31].

With aforementioned discussion, we selected the mixture of CB and SWCNTs as the nano-absorbers. Figure 3(e) presents an SEM microimage of the CB/SWCNT mixture and confirms this network structure (note that to clearly observe the morphology of the CB/SWCNT mixture, no PDMS resin was added here). By trial and error, the optimal CB/SWCNT weight ratio is determined to be 20:1. It is found the excessive SWCNT caused dramatical increase in viscosity of resin, making it difficult to spray in the following step. Then, different amounts of PDMS were blended with the CB/SWCNT absorbers. The reflectance spectra of the coatings with different amounts of PDMS, as shown in Fig. 3(f), indicate that higher filler contents (i.e., as PDMS:nano-absorber ≤ 50:21) favor the light absorption of the coating, in this case the av. hemispherical reflectance is less than 2%; however, the adhesion level with substate also decreases (Fig. S3(b) in the ESM), because of the nano-absorber could not be well wrapped by PDMS; small voids can be found on these coating surfaces, as confirmed by the SEM images (Fig. S3(a) in the ESM). Balancing the reflectance and adhesion level, we finally chose the formula, where PDMS:nano-absorber = 100:21. This formula shows a cross-cut adhesion level of 2 (0 is the best, 5 is the worst) with Al substrate (Fig. S3(b) in the ESM) and the av. hemispherical reflectance of ~ 3% (Fig. 3(f)), which represents the lowest level that can be obtained by the flat black coating in this work.

Since a portion of light can still be reflected by the flat black coating, building rough microstructures with regular protrusion on the coating surface to trap light and minimize light reflection is very necessary. Although some strategies have been proposed before, such as chemical vapor deposition (CVD), physical vapor

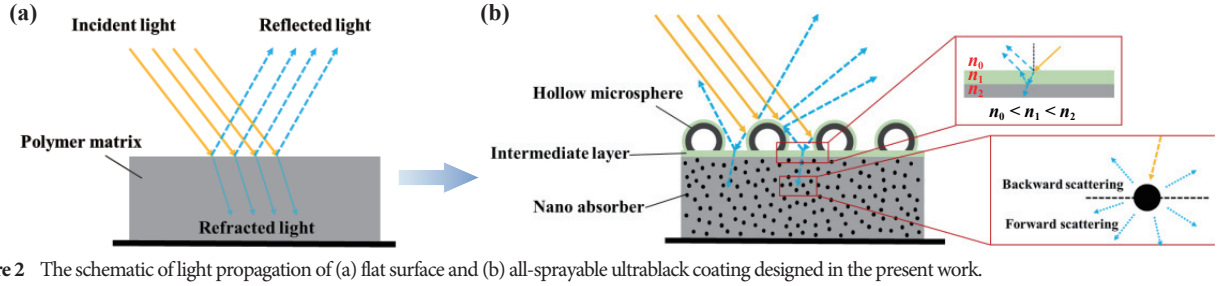

Figure 2 The schematic of light propagation of (a) flat surface and (b) all-sprayable ultrablack coating designed in the present work.

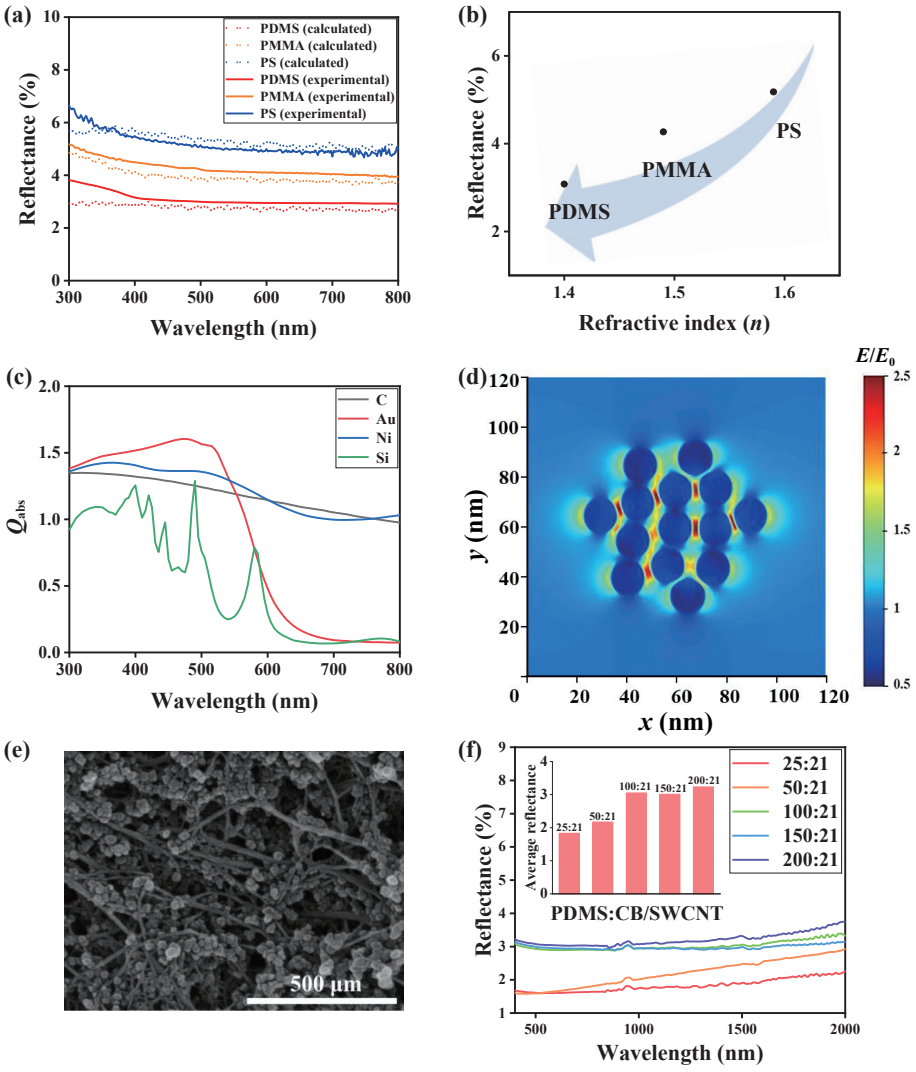

Figure 3 (a) The calculated and experimental reflectance spectra of different candidate polymers. (b) The av. reflectance of the candidate polymers. (c) The absorption coefficient (Q_{abs}) of C, Au, Ni, and Si particles, calculated by Mie theory (the particle diameter is 10 nm). (d) The scattering electric field distribution of carbon particles simulated by FDTD software (the wave vector is perpendicular to the *xy* plane). (e) SEM image of the mixed CB/SWCNT nano-absorbers, where weight ratio CB/SWCNT is 20:1. (f) The hemispherical reflectance spectra of the PDMS-based flat black coatings.

deposition (PVD), and template techniques, the spray coating has been seldom applied for micro-trap construction. This is because the micro-traps are usually difficult to build up by spray-coating process. However, we found the SiO_2 HMSs (with av. diameter of 13.4 μm and shell thickness of ~ 500 nm, Fig. S4 in the ESM) could be used for this purpose. The HMS shows lower density (0.51 g·cm^{-3}) than mixed dispersion, so they are apt to float onto coating top after spray coating and form rough and regular protrusion. This can be confirmed by the confocal microscopy and SEM images of the coating samples (Figs. 4(a)–4(d)). The flat coating without SiO_2 HMS is relatively smooth on the whole (Figs. 4(a) and 4(b)), whereas the coating with SiO_2 HMS becomes much rougher with hill-like undulation (Figs. 4(c) and 4(d)). The surface roughness, R_a, increases with HMS content rapidly at first, then becomes steady at higher content. R_a increases from 1.73 μm for the flat coating to over 6 μm for the HMS-containing coating (Fig. 4(e) and Figs. S5 and S6 in the ESM). However, at the excessive HMS content, the coating samples show some micro-voids on their surfaces (Fig. S7(a) in the ESM), suggesting the insufficient wrapping of the PDMS resin. The magnified SEM images (Fig. S7(b) in the ESM) support this point, where the HMS surface is only partially covered by PDMS resin, the rest part is nearly bare. Figure 4(f) gives the hemispherical reflectance spectra of the coating with/without HMS tested in the wavelength range from 400 to 2000 nm. The av. hemispherical reflectance changes non-linearly with HMS content, the lowest value (~ 2.1%) is found when 0.2 g of HMS was added to the coating. The rough surface, likely acting as light micro-traps, is able to enhance multiple scattering of light, and thus minimizing the total light reflection (Fig. 2(b)). Ray tracing simulation (Fig. S8 in the ESM) also proves that a surface with spherical microspheres possesses lower reflectance than the flat coating via multiple scattering effect. Further increase in HMS content, however, increases the reflectance of the coatings. The reason might be ascribed to the expose of the highly-reflective HMS, which was not well wrapped by the PDMS resin (Fig. S7(b) in the ESM). In addition, Fig. 4(g) reveals the normalized hemispherical reflectance of coating filled with HMS (sample: HMS-0.2) is not sensitive to the incident angle, in obvious contrast with the significant increase for the flat coating.

The hemispherical reflection is a sum of specular and diffuse reflection in terms of energy, it does not describe the scattering behavior of a surface. The scattering performance for an opaque surface is generally characterized by the bidirectional reflection distribution function (BRDF) [46–48], which describes how an incident light propagates and diffuses after being reflected by a surface. BRDF value can be understood as the intensity of scattering light in a certain direction caused by the incident

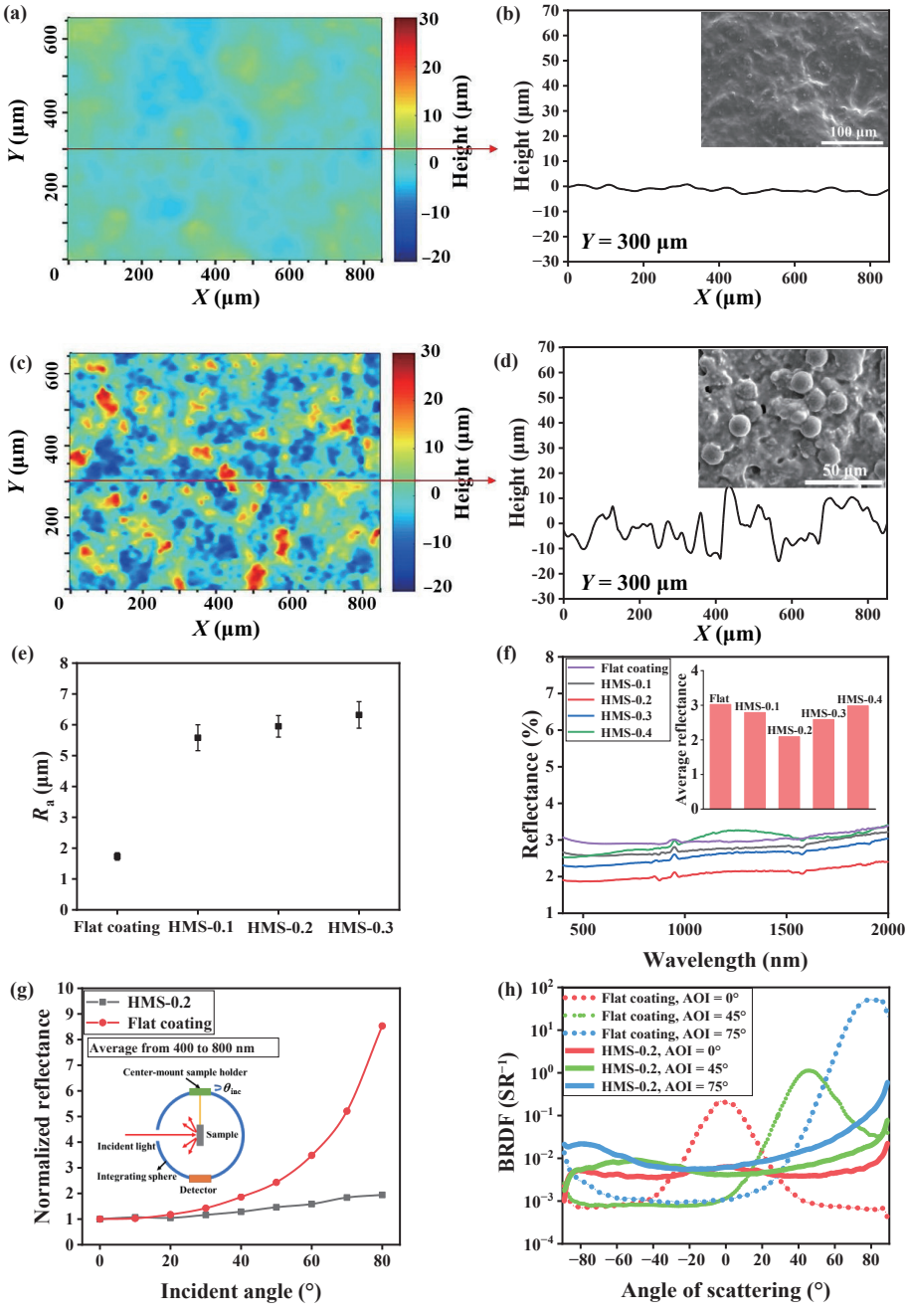

Figure 4 Confocal microscopy images of coatings (a) without SiO_2 HMS and (c) with SiO_2 HMS. ((b) and (d)) Height map of the profiles marked in ((a) and (c)); insets show SEM images of the relevant coatings. (e) Surface roughness, R_a, of the coating with different amount of HMS. (f) The hemispherical reflectance spectra of different coatings (the inset shows average reflectance from 400 to 2000 nm). (g) Normalized multi-angle hemispherical reflectance (all data are normalized with respect to the reflectance at normal incidence) of coatings. (h) Scattering performance of different coatings at angle of incidence (AOI) of 0°, 45°, and 75°; the wavelength of incident light is 532 nm (the angle of scattering is positive when scattered light and incident light are on the same side of normal).

luminous flux per unit; the smaller the BRDF, the weaker the intensity of scattering light in the corresponding direction (Fig. S9 in the ESM). Figure 4(h) compares in-plane BRDF spectra of HMS-0.2 sample and flat sample, which were measured at various angles of scattering (AOS). The most of BRDF values of HMS-0.2 sample are stable at 10^{-2} sr^{-1}, and the curves are relatively flat, showing a near-Lambertian scattering behavior. This implies that the visual perception of the HMS-0.2 sample is very similar when observed from different directions. By sharp contrast, although the flat black coating sample shows the very small BRDF values (around 10^{-3} sr^{-1}) somewhere, it exhibits a strong specular peak with much higher BRDF values (10^{-1}–10^{1} sr^{-}). The larger the incident angle, the higher the peak. Therefore, the flat sample is highly reflected when observed from large angle. This result confirms that the HMS on coating surface can also form numerous scattering centers and promote uniform distribution of the reflected light, as illustrated in Fig. 2(b).

The rough coating surface built up by introduction of HMS resulted in ~ 1% decline in reflectance (Fig. 4(f)), as compared with the flat coating, i.e. the reflectance reached ~ 2%. This value, however, would not satisfy fully the strict requirements of many applications, such as stray light suppression, where the high absorption and low reflection of materials are essential. To further minimize the reflectance of the coating, we introduce an intermediate layer onto the coating surface. According to Fresnel law, the intermediate layer, the RI value of which is between those of coating matrix and air, is able to reduce the interfacial reflection effectively. Here, the PFMS is selected because its RI tested by the ellipsometer is 1.19–1.32 at 300–800 nm (Fig. S10 in the ESM), whereas the PDMS has the ~ 1.4 of RI in the same wavelength

band [49]. The PFMS ethanol solution can be directly sprayed onto the coating surface, then undergo hydrolysis under humidity and self-assembled into thin polymer layer (Fig. S11 in the ESM). Energy disperse spectroscopy (Fig. 5(a)) confirms fluorine is uniformly distributed on the coating surface; the fluorine peak is also detected using X-ray photoelectron spectroscopy (XPS) (Fig. 5(b)), as indicated by the arrow. Figure 5(c) presents the reflectance spectra of the coating samples before and after application of the PFMS intermediate, where the samples are labeled as HMS-0.2@F-No., the "No." represents the cycle of spraying. All the treated coating samples show ~ 0.8% reduction in hemispherical reflectance, the lowest reflectance is 0.94% for sample HMS-0.2@F-3. Surprisingly, this reflectance reduction is independent on the spraying cycle. So far, correlation of coating reflectance with PFMS layer thickness is impossible, because the PFMS layer is too thin to be measured by SEM or its mass fraction is very small and cannot be estimated by thermogravimetric analysis (TGA). It is speculated that only a small part of PFMS molecules can react with the active groups on coating surface and form monolayer structure [50]; as these active groups are depleted, the left un-reacted PFMS will gradually evaporate during thermal cure, therefore the thickness of PFMS could be constant regardless of the spraying cycle. In addition, there are no obvious interference absorption peaks for all samples in Fig. 5(c), suggesting reduction in reflectance is mainly due to the interfacial anti-reflection based on Fresnel law, not the interference effect.

Figure S12(a) in the ESM illustrates the basic model of the coating in the present work, here we assumed: i) No occurrence of the interference effect, because the coating surface is very rough, does not meet the interference conditions; and the results in Fig. 5(c) also show no interference peak; ii) light absorption of the intermediate layer is neglected due to its small κ value and thickness. According to Fresnel law, we proved that if a surface of higher RI (n_2) is coated with an intermediate layer of lower RI (n_1), the total reflectance (R_{double}) from two interfaces (Eq. S(3)) is always lower than the reflectance of the individual surface (R_{single}). Figure S12(b) in the ESM depicts the variation of R_{sum} as a function of n_1 and n_2. It can be seen that at a given n_2, a specific n_1 value exists, where the model realizes the lowest R_{double}. In our case, as n_2 = 1.4 (PDMS), the calculated specific n_1 should be 1.18 (Fig. S12(c) in the ESM), which is close to the av. RI for PFMS (~ 1.28, see Fig. S10 in the ESM). That is why the PFMS intermediate presents significant anti-interfacial reflection. The introduction of intermediate layer of lower RI between surface and air seems a universal method to suppress reflection. For example, we deposited MgF_2 (RI = 1.38 [51]) intermediate layer onto the HMS-0.2 coating by electron beam evaporation, the reflectance of coating decreases from 1.8% to 1.1%, as summarized in Fig. S13 in the ESM. Another example: We spray-coated the PFMS intermediate layer onto HMS-containing black epoxy coating and found similar tendency as described above (Fig. S14 in the ESM; RI of epoxy is around 1.6 [52]), the reflectance decreased significantly from 4.91% to 2.81%.

In sum, through the aforementioned comprehensive effects, the hemispherical reflectance of sample HMS-0.2@F-3 can decrease down to ~ 1% over VIS–NIR band (Fig. 5(c)), showing weak dependence on the incident light wavelength. The ultra-blackness also extends to NIR–MIR (MIR: mid-infrared) wavelength (2 ~ 20 μm), where av. R is ~2% (Fig. 5(d)). Moreover, the thin PFMS layer has little effect on the scattering performance, showing slightly reduced BRDF values in comparison with the original coating (Fig. 5(e)).

In appearance, our ultrablack coating is much blacker than the commercially-available black paint Z306, which is commonly-used in optical systems (Fig. 6(a)). The ultrablack coatings can be applied to complex curved surfaces (Fig. 6(b), Fig. S16 in the ESM, and Video ESM2) and achieved cross-cut adhesion grade of 1 with various substrates (Fig. S15 in the ESM). Table S2 in the ESM summarizes some recent works on ultrtablack materials in literature. Compared the previous works with ours, most ultrablack materials are realized by using complicated equipment and/or tedious process, this may limit their applications in large scale. There are some sprayable coatings in Table S2 in the ESM, which show excellent ultrablack performance [31, 53, 54]. However, after carefully reading the works, we found those materials usually comprise very high content of light absorbers (over 95 wt.%) but very low content of binder or even no binder,

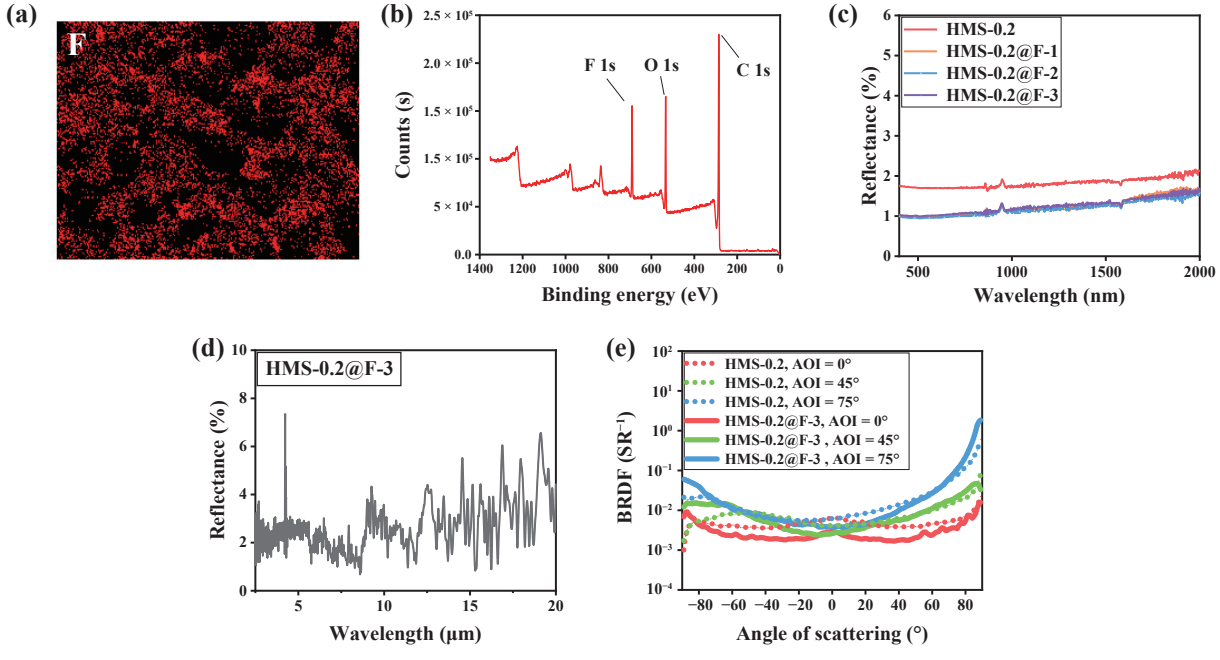

Figure 5 Sample HMS-0.2 coated with low RI PFMS intermediate layer: (a) energy dispersive spectroscopy (EDS) and (b) XPS; (c) hemispherical reflectance spectra at VIS–NIR wavelength of samples with/without PFMS intermediate layer, (d) hemispherical reflective spectrum at NIR–MIR wavelength of the sample HMS-0.2@F-3, (e) scattering performance of HMS-0.2 and HMS@F-3 at various AOI (0°, 45°, and 75°); the wavelength of incident light is 532 nm.

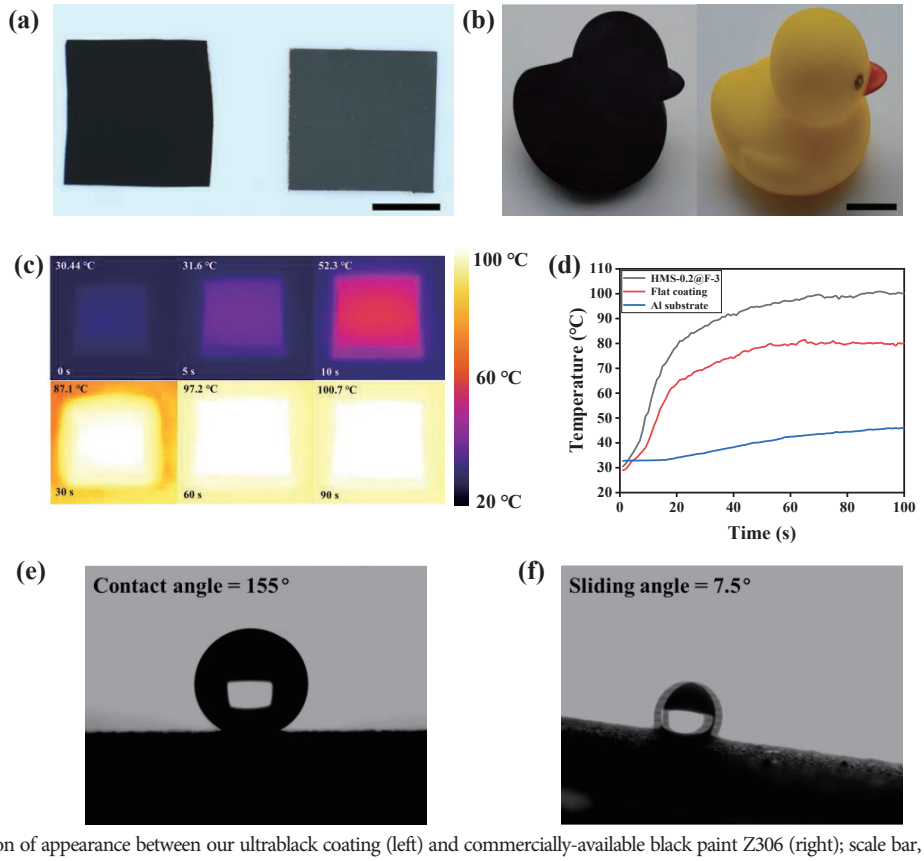

Figure 6 (a) Comparison of appearance between our ultrablack coating (left) and commercially-available black paint Z306 (right); scale bar, 2 cm. (b) A yellow duck toy before and after spray-coating, demonstrating the ultrablack coating can be applied to complex curved surface; scale bar, 1 cm. (c) Infrared thermal images of samples at various illumination time and (d) related curves of temperature vs. illumination. (e) Water contact angle and (f) sliding angle of the HMS-0.2@F-3.

therefore the adhesion with substrate could not be acceptable. Comparatively, owing to that light extinction effects are decoupled to different coating layers, our sample (HMS-0.2@F-3) has relatively higher content of polymer binder (weight ratio is ~ 66%), ensuring the good adhesion and basic mechanical robustness.

The excellent light absorption performance makes our materials promising for solar energy harvesting. Figure 6(c) presents the infrared thermal images of samples illuminated under a standard power density of 1000 W·m^{-2} with standard level A. The surface temperature of HMS-0.2@F-3 rises rapidly and reaches the balanced temperature of 90 °C in ~ 30 s; the temperature distribution is uniform over the entire sample surface. For comparison, the flat black coating and Al substrate have lower temperature rising rates and lower balanced temperatures under the same illumination condition (Fig. 6(d)). The photothermal effect of the sample HMS-0.2@F-3 is stable after several cycles of illumination (Fig. S17 in the ESM). Additionally, owing to the low surface energy of PFMS and rough topography, the HMS-0.2@F-3 ultrablack coating possesses the 155° of water contact angle and 7.5° of sliding angle (Figs. 6(e) and 6(f)), showing somewhat superhydrophobicity, benefiting its self-cleaning (Video ESM3) as well as outdoor application.

4 Conclusions

In summary, the ultrablack coating was designed and prepared by simple and efficient spray-coating technique in the present work. Comprehensive light extinction mechanisms were utilized here, including enhancing light intrinsic absorption of matrix by addition of carbon nanoparticles, constructing micro light traps/scattering centers by addition of micro hollow spheres, as well as minimizing the interfacial reflection by introducing the fluorine-containing low RI intermediate. The optimized coating exhibited extremely-low hemispherical reflectance over a broadband wavelength from 0.4 to 20 μm (i.e., $R \approx 1\%$ in VIS wavelength and $R \approx 2\%$ in NIR-MIR wavelength), excellent multi-angle scattering ability (BRDF = 10^{-2}–10^{-3} sr^{-1}) without any specular peaks, good adhesion grade with various substrates, and self-cleaning feature, and was effective in solar thermal harvest test. Owing to the simple process and excellent performance, this all-sprayable ultrablack coating may have a great chance to replace some ultrablack surfaces manufactured by complicated techniques. The design idea should be useful for other material systems also.

Acknowledgements

This work was jointly supported by the National Natural Science Foundation of China (Nos. 11832010, 11890682 and 21721002), the National Key Basic Research Program of China (No. 2018YFA0208403), and the Austrian-Chinese Cooperative Research and Development Projects (No. GJHZ2043), Chinese Academy of Sciences.

Electronic Supplementary Material: Supplementary material (simulation of Mie scattering and FDTD, SEM surface morphologies, statistical histogram of SiO_2, confocal microscopy images, ray tracing simulation, schematic diagram of BRDF test and self-assembly process, refractive index of materials, calculation of interface reflection based on Fresnel law, EDS maps, cross-cut adhesion test, comparison of some reported ultrablack surfaces, and nomination and formula of samples) is available in the online version of this article at https://doi.org/10.1007/s12274-023-5590-5.

References

[1] Theocharous, E.; Chunnilall, C. J.; Mole, R.; Gibbs, D.; Fox, N.; Shang, N. G.; Howlett, G.; Jensen, B.; Taylor, R.; Reveles, J. R. et al. The partial space qualification of a vertically aligned carbon nanotube coating on aluminium substrates for EO applications. *Opt. Express* **2014**, *22*, 7290–7307.

[2] Akutsu, T.; Saito, Y.; Sakakibara, Y.; Sato, Y.; Niwa, Y.; Kimura, N.; Suzuki, T.; Yamamoto, K.; Tokoku, C.; Koike, S. et al. Vacuum and cryogenic compatible black surface for large optical baffles in advanced gravitational-wave telescopes. *Opt. Mater. Express* **2016**, *6*, 1613–1626.

[3] Lehman, J.; Theocharous, E.; Eppeldauer, G.; Pannell, C. Gold-black coatings for freestanding pyroelectric detectors. *Meas. Sci. Technol.* **2003**, *14*, 916–922.

[4] Lehman, J.; Sanders, A.; Hanssen, L.; Wilthan, B.; Zeng, J. N.; Jensen, C. Very black infrared detector from vertically aligned carbon nanotubes and electric-field poling of lithium tantalate. *Nano Lett.* **2010**, *10*, 3261–3266.

[5] Selvakumar, N.; Krupanidhi, S. B.; Barshilia, H. C. Carbon nanotube-based tandem absorber with tunable spectral selectivity: Transition from near-perfect blackbody absorber to solar selective absorber. *Adv. Mater.* **2014**, *26*, 2552–2557.

[6] Li, P. F.; Liu, B. A.; Ni, Y. Z.; Liew, K. K.; Sze, J.; Chen, S.; Shen, S. Large-scale nanophotonic solar selective absorbers for high-efficiency solar thermal energy conversion. *Adv. Mater.* **2015**, *27*, 4585–4591.

[7] Tu, C.; Cai, W. F.; Chen, X.; Ouyang, X. L.; Zhang, H.; Zhang, Z. A 3D-structured sustainable solar-driven steam generator using super-black nylon flocking materials. *Small* **2019**, *15*, 1902070.

[8] Wang, H. Q.; Zhang, C.; Ji, X. J.; Yang, J. M.; Zhang, Z. H.; Ma, Y.; Zhang, Z. H.; Zhou, B.; Shen, J.; Du, A. Over 11 $kg \cdot m^{-2} \cdot h^{-1}$ evaporation rate achieved by cooling metal–organic framework foam with pine needle-like hierarchical structures to subambient temperature. *ACS Appl. Mater. Interfaces* **2022**, *14*, 10257–10266.

[9] Meng, T. T.; Li, Z. T.; Wan, Z. M.; Zhang, J.; Wang, L. Z.; Shi, K. J.; Bu, X. T.; Alshehri, S. M.; Bando, Y.; Yamauchi, Y. et al. MOF-Derived nanoarchitectured carbons in wood sponge enable solar-driven pumping for high-efficiency soil water extraction. *Chem. Eng. J.* **2023**, *452*, 139193.

[10] Peng, L.; Liu, D. Q.; Cheng, H. F.; Zhou, S.; Zu, M. A multilayer film based selective thermal emitter for infrared stealth technology. *Adv. Opt. Mater.* **2018**, *6*, 1801006.

[11] Li, Y.; Bai, X.; Yang, T. Z.; Luo, H. L.; Qiu, C. W. Structured thermal surface for radiative camouflage. *Nat. Commun.* **2018**, *9*, 273.

[12] Huang, Y. J.; Pu, M. B.; Zhao, Z. Y.; Li, X.; Ma, X. L.; Luo, X. G. Broadband metamaterial as an "invisible" radiative cooling coat. *Opt. Commun.* **2018**, *407*, 204–207.

[13] Wang, G.; Xing, F.; Wei, M. S.; You, Z. Rapid optimization method of the strong stray light elimination for extremely weak light signal detection. *Opt. Express* **2017**, *25*, 26175–26185.

[14] Mizuno, K.; Ishii, J.; Kishida, H.; Hayamizu, Y.; Yasuda, S.; Futaba, D. N.; Yumura, M.; Hata, K. A black body absorber from vertically aligned single-walled carbon nanotubes. *Proc. Natl. Acad. Sci. USA* **2009**, *106*, 6044–6047.

[15] Yang, Z. P.; Hsieh, M. L.; Bur, J. A.; Ci, L. J.; Hanssen, L. M.; Wilthan, B.; Ajayan, P. M.; Lin, S. Y. Experimental observation of extremely weak optical scattering from an interlocking carbon nanotube array. *Appl. Opt.* **2011**, *50*, 1850–1855.

[16] Tao, H. Y.; Lin, J. Q.; Hao, Z. Q.; Gao, X.; Song, X. W.; Sun, C. K.; Tan, X. Formation of strong light-trapping Nano- and microscale structures on a spherical metal surface by femtosecond laser filament. *Appl. Phys. Lett.* **2012**, *100*, 201111.

[17] Zhou, L.; Tan, Y. L.; Ji, D. X.; Zhu, B.; Zhang, P.; Xu, J.; Gan, Q. Q.; Yu, Z. F.; Zhu, J. Self-assembly of highly efficient, broadband plasmonic absorbers for solar steam generation. *Sci. Adv.* **2016**, *2*, e1501227.

[18] Zhou, L.; Tan, Y. L.; Wang, J. Y.; Xu, W. C.; Yuan, Y.; Cai, W. S.; Zhu, S. N.; Zhu, J. 3D self-assembly of aluminium nanoparticles for plasmon-enhanced solar desalination. *Nat. Photonics* **2016**, *10*, 393–398.

[19] Wattoo, A. G.; Bagheri, R.; Ding, X. F.; Zheng, B. Z.; Liu, J. K.; Xu, C.; Yang, L. J.; Song, Z. L. Template free growth of robustly stable nanophotonic structures: Broadband light superabsorbers. *J. Mater. Chem. C* **2018**, *6*, 8646–8662.

[20] Chen, Y. L.; Zhao, G. M.; Ren, L. P.; Yang, H. J.; Xiao, X. F.; Xu, W. L. Blackbody-inspired array structural polypyrrole-sunflower disc with extremely high light absorption for efficient photothermal evaporation. *ACS Appl. Mater. Interfaces* **2020**, *12*, 46653–46660.

[21] Amemiya, K.; Koshikawa, H.; Imbe, M.; Yamaki, T.; Shitomi, H. Perfect blackbody sheets from nano-precision microtextured elastomers for light and thermal radiation management. *J. Mater. Chem. C* **2019**, *7*, 5418–5425.

[22] Ci, L. J.; Vajtai, R.; Ajayan, P. M. Vertically aligned large-diameter double-walled carbon nanotube arrays having ultralow density. *J. Phys. Chem. C* **2007**, *111*, 9077–9080.

[23] Brown, R. J. C.; Brewer, P. J.; Milton, M. J. T. The physical and chemical properties of electroless nickel-phosphorus alloys and low reflectance nickel-phosphorus black surfaces. *J. Mater. Chem.* **2002**, *12*, 2749–2754.

[24] Lin, H.; Ouyang, M. Z.; Chen, B. X.; Zhu, Q. F.; Wu, J. S.; Lou, N.; Dong, L. T.; Wang, Z. B.; Fu, Y. G. Design and fabrication of moth-eye subwavelength structure with a waist on silicon for broadband and wide-angle anti-reflection property. *Coatings* **2018**, *8*, 360.

[25] Yang, Z. P.; Ci, L.; Bur, J. A.; Lin, S. Y.; Ajayan, P. M. Experimental observation of an extremely dark material made by a low-density nanotube array. *Nano Lett.* **2008**, *8*, 446–451.

[26] Kanamori, Y.; Sasaki, M.; Hane, K. Broadband antireflection gratings fabricated upon silicon substrates. *Opt. Lett.* **1999**, *24*, 1422–1424.

[27] Ng, C.; Yap, L. W.; Roberts, A.; Cheng, W. L.; Gómez, D. E. Black gold: Broadband, high absorption of visible light for photochemical systems. *Adv. Funct. Mater.* **2017**, *27*, 1604080.

[28] Lehman, J.; Yung, C.; Tomlin, N.; Conklin, D.; Stephens, M. Carbon nanotube-based black coatings. *Appl. Phys. Rev.* **2018**, *5*, 011103.

[29] Gokhale, V. J.; Shenderova, O. A.; Mcguire, G. E.; Rais-Zadeh, M. Infrared absorption properties of carbon nanotube/nanodiamond based thin film coatings. *J. Microelectromech. Syst.* **2013**, *23*, 191–197.

[30] Wei, W. Y.; Li, M. W.; Han, Y.; Wu, M. J.; Yan, J.; Liu, M. J.; Chen, Y. L. Flexible and robust ultrablack elastomers with a dual-gradient design for broadband and efficient light management. *Adv. Opt. Mater.* **2022**, *10*, 2101854.

[31] Jin, Y. H.; Zhang, T. F.; Zhao, J.; Zhao, Y. X.; Li, C.; Song, J.; Hao, X. P.; Wang, J. P.; Jiang, K. L.; Fan, S. S. et al. Spray coating of a perfect absorber based on carbon nanotube multiscale composites. *Carbon* **2021**, *178*, 616–624.

[32] Wang, H. Q.; Du, A.; Ji, X. J.; Zhang, C.; Zhou, B.; Zhang, Z. H.; Shen, J. Enhanced photothermal conversion by hot-electron effect in ultrablack carbon aerogel for solar steam generation. *ACS Appl. Mater. Interfaces* **2019**, *11*, 42057–42065.

[33] Li, H. M.; Chen, Y. F.; Wang, P. D.; Xu, B. S.; Ma, Y. B.; Wen, W. B.; Yang, Y. Z.; Fang, D. N. Porous carbon-bonded carbon fiber composites impregnated with SiO_2–Al_2O_3 aerogel with enhanced thermal insulation and mechanical properties. *Ceram. Int.* **2018**, *44*, 3484–3487.

[34] Yu, Y. L.; Chen, S.; Jia, Y.; Qi, T.; Xiao, L.; Cui, X.; Zhuang, D. M.; Wei, J. Q. Ultra-black and self-cleaning all carbon nanotube hybrid films for efficient water desalination and purification. *Carbon* **2020**, *169*, 134–141.

[35] Wang, B. B.; Li, D. H.; Tang, M. W.; Ma, H. B.; Gui, Y. G.; Tian, X.; Quan, F. Y.; Song, X. Q.; Xia, Y. Z. Alginate-based hierarchical porous carbon aerogel for high-performance supercapacitors. *J. Alloys Compd.* **2018**, *749*, 517–522.

[36] Sun, W.; Du, A.; Feng, Y.; Shen, J.; Huang, S. M.; Tang, J.; Zhou, B. Super black material from low-density carbon aerogels with subwavelength structures. *ACS Nano* **2016**, *10*, 9123–9128.

[37] Wattoo, A. G.; Xu, C.; Yang, L. J.; Ni, C. L.; Yu, C.; Nie, X.; Yan, M. S.; Mao, S. D.; Song, Z. L. Design, fabrication and thermal stability of spectrally selective TiAlN/SiO_2 tandem absorber. *Sol.*

Energy **2016**, *138*, 1–9.
[38] Tsao, S. H.; Wan, D. H.; Lai, Y. S.; Chang, H. M.; Yu, C. C.; Lin, K. T.; Chen, H. L. White-light-induced collective heating of gold nanocomposite/*Bombyx mori* silk thin films with ultrahigh broadband absorbance. *ACS Nano* **2015**, *9*, 12045–12059.
[39] Hedayati, M. K.; Javaherirahim, M.; Mozooni, B.; Abdelaziz, R.; Tavassolizadeh, A.; Chakravadhanula, V. S. K.; Zaporojtchenko, V.; Strunkus, T.; Faupel, F.; Elbahri, M. Design of a perfect black absorber at visible frequencies using plasmonic metamaterials. *Adv. Mater.* **2011**, *23*, 5410–5414.
[40] Gittleson, F. S.; Hwang, D.; Ryu, W. H.; Hashmi, S. M.; Hwang, J.; Goh, T.; Taylor, A. D. Ultrathin nanotube/nanowire electrodes by spin-spray layer-by-layer assembly: A concept for transparent energy storage. *ACS Nano* **2015**, *9*, 10005–10017.
[41] Majumder, M.; Rendall, C.; Li, M.; Behabtu, N.; Eukel, J. A.; Hauge, R. H.; Schmidt, H. K.; Pasquali, M. Insights into the physics of spray coating of SWNT films. *Chem. Eng. Sci.* **2010**, *65*, 2000–2008.
[42] Lin, S.; Wang, H. Y.; Zhang, X. N.; Wang, D.; Zu, D.; Song, J. N.; Liu, Z. L.; Huang, Y.; Huang, K.; Tao, N. et al. Direct spray-coating of highly robust and transparent Ag nanowires for energy saving windows. *Nano Energy* **2019**, *62*, 111–116.
[43] Mulay, M. R.; Chauhan, A.; Patel, S.; Balakrishnan, V.; Halder, A.; Vaish, R. Candle soot: Journey from a pollutant to a functional material. *Carbon* **2019**, *144*, 684–712.
[44] Khodasevych, I. E.; Wang, L. P.; Mitchell, A.; Rosengarten, G. Micro- and nanostructured surfaces for selective solar absorption. *Adv. Opt. Mater.* **2015**, *3*, 852–881.
[45] Torres, J. F.; Tsuda, K.; Murakami, Y.; Guo, Y. F.; Hosseini, S.; Asselineau, C. A.; Taheri, M.; Drewes, K.; Tricoli, A.; Lipiński, W. et al. Highly efficient and durable solar thermal energy harvesting via scalable hierarchical coatings inspired by stony corals. *Energy Environ. Sci.* **2022**, *15*, 1893–1906.
[46] Leloup, F. B.; Forment, S.; Dutré, P.; Pointer, M. R.; Hanselaer, P. Design of an instrument for measuring the spectral bidirectional scatter distribution function. *Appl. Opt.* **2008**, *47*, 5454–5467.
[47] Zheng, Z. R.; Zhou, J.; Gu, P. F. Roughness characterization of well-polished surfaces by measurements of light scattering distribution. *Opt. Appl.* **2010**, *40*, 811–818.
[48] Balling, B. A comparative study of the bidirectional reflectance distribution function of several surfaces as a mid-wave infrared diffuse reflectance standard. Ohio: Department of Engineering Physics, Air Force Institute of Technology, 2009.
[49] Zhang, X. N.; Qiu, J.; Li, X. C.; Zhao, J. M.; Liu, L. H. Complex refractive indices measurements of polymers in visible and near-infrared bands. *Appl. Opt.* **2020**, *59*, 2337–2344.
[50] Hozumi, A.; Takai, O. Effect of hydrolysis groups in fluoro-alkyl silanes on water repellency of transparent two-layer hard-coatings. *Appl. Surf. Sci.* **1996**, *103*, 431–441.
[51] Dodge, M. J. Refractive properties of magnesium fluoride. *Appl. Opt.* **1984**, *23*, 1980–1985.
[52] Guan, C.; Lü, C. L.; Liu, Y. F.; Yang, B. Preparation and characterization of high refractive index thin films of TiO_2/epoxy resin nanocomposites. *J. Appl. Polym. Sci.* **2006**, *102*, 1631–1636.
[53] Guo, J.; Li, D. D.; Zhao, H.; Zou, W. Z.; Yang, Z. S.; Qian, Z. C.; Yang, S. J.; Yang, M.; Zhao, N.; Xu, J. Cast-and-use super black coating based on polymer-derived hierarchical porous carbon spheres. *ACS Appl. Mater. Interfaces* **2019**, *11*, 15945–15951.
[54] Guo, J.; Li, D. D.; Qian, Z. C.; Luo, H.; Yang, M.; Wang, Q. X.; Xu, J.; Zhao, N. Carbon vesicles: A symmetry-breaking strategy for wide-band and solvent-processable ultrablack coating materials. *Adv. Funct. Mater.* **2020**, *30*, 1909877.